Tunable Weyl half-semimetals in two-dimensional iron-based materials MFeSe (M = Tl, In, Ga)

Hao Huan [1,2] Yang Xue,[1,3] Bao Zhao,[1,4] Hairui Bao,[1,2] Lei Liu,[1,2] and Zhongqin Yang [1,2,*]

[1]*State Key Laboratory of Surface Physics and Key Laboratory of Computational Physical Sciences (MOE)*
& Department of Physics, Fudan University, Shanghai 200433, China
[2]*Shanghai Qi Zhi Institute, Shanghai 200030, China*
[3]*School of Science, East China University of Science and Technology, Shanghai 200237, China*
[4]*School of Physics Science and Information Technology, Shandong Key Laboratory of Optical Communication Science and Technology,*
Liaocheng University, Liaocheng 252059, China

The layered iron chalcogenide materials have attracted considerable attention recently for their exotic superconductivity at relatively high temperatures. Topological phases are, however, seldom proposed in these materials. Based on density-functional theory calculations together with symmetry analysis, 100% spin-polarized Weyl semimetals, namely Weyl half semimetals (WHSMs), are predicted in two-dimensional (2D) TlFeSe and GaFeSe monolayers, built based on FeSe monolayers. The acquired Weyl fermions are protected by a nonsymmorphic symmetry. Dissimilarly, the InFeSe monolayer is found to be a quantum anomalous Hall (QAH) insulator with a large band gap (403 meV). By tuning the magnetization direction, the monolayers can vary from a WHSM to a QAH insulator or vice versa. The phase-transition mechanism is analyzed by using an effective $\mathbf{k} \cdot \mathbf{p}$ model. Our work provides a pathway to carry out the fascinating 2D WHSMs and the QAH effect in one material which will have promising applications in not only spintronics but also topological microelectronics.

I. INTRODUCTION

Two-dimensional (2D) materials provide an appealing platform for creating a new generation of microelectronic and spintronic devices, including novel information storage and logic devices, etc. [1–5]. Compared to traditional microelectronic devices, spintronic devices have several advantages such as faster processing speeds, higher integration densities, and lower power consumption [3,6]. Weyl semimetals that have crossing linear bands with degenerate points (Weyl points) at the Fermi level (E_F), like the Dirac cones in graphene, have been a hot topic in recent years [7–10]. Such materials can possess very unique features, such as Fermi arc surface states, chiral anomaly, anomalous Hall effect, and large negative magnetoresistance [8,10]. Based on the relatively mature studies of the Weyl semimetals in the three-dimensional material [7–10], Weyl half semimetals (WHSMs) have been proposed in 2D materials [11–13], in which the time-reversal symmetry is broken and the Weyl points at the E_F belong to a single-spin channel. For example, in 2019, You *et al.* first proposed PtCl$_3$ monolayers as a 2D WHSM [11]. After that, the states were reported in some ferrovalley materials of RuBr$_2$ [14] and VSi$_2$N$_4$ [15]. Since WHSMs combine the half-metallic ferromagnetism (FM) and Weyl fermions, they have potential applications in not only topological microelectronics but also spintronics. These exotic WHSMs are, however, not generally available in 2D systems. A series of previous studies have indicated that spin-orbit

coupling (SOC) interactions in the systems can cause the breakdown of the Weyl states with band gaps opened [16,17]. Additionally, compared to the three-dimensional materials, the lower symmetry of the 2D systems makes the appearance of the Weyl points difficult, which are usually protected by certain symmetries in the systems. It is meaningful to explore new rare 2D materials with the fascinating WHSM states.

Over the past decade, the layered iron chalcogenide materials have attracted much attention in both theoretical and experimental studies due to their tempting superconducting behaviors [18–25]. Layered FeSe compounds held together through weak van der Waals interactions are the parent materials in this direction. The bulk FeSe could be intercalated with metal atoms such as Tl, K, and Li between the layers [19–22], showing superconductivity at temperatures between 31 and 43 K. For FeSe thin films, the superconductivity critical temperatures could be increased. For example, the FeSe films were fabricated on bilayer graphene and the superconductivity transition temperature was found scaling inversely with film thickness in the system [18]. And, superconductivity was observed above 100 K in the single-layer FeSe films grown on a doped SrTiO$_3$ substrate [25]. Thus, FeSe films have rich physical connotations, in which topological phases are, however, rarely reported until now. With the technique of molecular-beam epitaxy [18,24,25], the FeSe monolayers actually become a new material platform, which may be designed to explore the interesting 2D topological electronic states such as Weyl semimetals, quantum anomalous Hall effects [26,27], and quantum spin Hall effects [28–30], etc.

In this work, by using first-principles calculations and an effective $\mathbf{k} \cdot \mathbf{p}$ model, we propose a family of 2D

*zyang@fudan.edu.cn

monolayers materials called MFeSe (M = Tl, In, Ga), based on the pristine FeSe monolayer [23,24,31–33]. The TlFeSe and GaFeSe monolayers are found to be WHSMs, while the InFeSe monolayer is a QAH insulator. Very importantly, all three proposed materials with dynamical and thermal stability have FM ground states with very high Curie temperatures (T_c) (up to 1280 K), beneficial to experimental observation and practical applications. The TlFeSe and GaFeSe monolayers have fully spin-polarized Weyl points with a high Fermi velocity (4.24×10^5 ms^{-1}), primarily composed of Fe d_{xy} and $d_{x^2-y^2}$ orbitals. The Weyl points located along the Γ-X path in the Brillouin zone (BZ) are protected by nonsymmorphic symmetries. The appearance of the Weyl points is rationalized well by an effective $\boldsymbol{k} \cdot \boldsymbol{p}$ model. The MFeSe monolayer can switch between the WHSM state and the QAH state by tuning the magnetization direction. Our findings provide ideal material candidates for 2D high-temperature WHSMs and QAH insulators, which show great potential in the applications of low-power consumption spintronic devices with high performance.

II. METHODS

The first-principles density-functional theory (DFT) method [34–36] is employed to investigate the electronic properties of the monolayer materials. The advanced hybrid functional of Heyd-Scuseria-Ernzerhof method (HSE06) [37] is chosen for the structural relaxation and electronic structure calculations, which together with the many successful examples of DFT calculations for the similar electronic states and materials [26,38–41] guarantees the reliability of the results predicted in this work. The plane-wave basis with a kinetic energy cutoff of 500 eV is employed. The first BZ is sampled by the Γ-centered Monkhorst-Pack grids of $13 \times 13 \times 1$ [42]. The vacuum layer is set to 20 Å to avoid the coupling between the periodic layers. All the atoms are allowed to relax until the atomic force on each atom is smaller than 0.01 eV/Å. The convergence criterion for the total energies is set to be 10^{-6} eV. The phonon spectra are performed by using density-functional perturbation theory as implemented in the PHONOPY code [43]. The first-principles molecular-dynamics (MD) simulations are performed with a $4 \times 4 \times 1$ supercell by using Nosé-Hoover thermostat at 300 K. Surface states are calculated with WANNIER90 [44] and WANNIERTOOLS [45] packages. To estimate the T_c of the FM states, the Monte Carlo simulations [46] are performed on a 51×51 supercell with 10^6 steps at each temperature.

III. RESULTS AND DISCUSSION

A. Structural stabilities and FM ground states

The MFeSe (M = Tl, In, Ga) monolayers, built based on the FeSe single layer, have a layered tetragonal crystal structure (space group $P4/nmm$, No. 129), the same as that of the FeSe single layer [33,47,48]. As illustrated in Figs. 1(a)–1(c), the MFeSe monolayer has two Fe atoms per unit cell, lying on the same plane in the unit cell, while the nonmagnetic M and Se atoms are located on both sides of the center plane in a staggered order. The calculated lattice constants [Fig. 1(d)] for the TlFeSe, InFeSe, and GaFeSe monolayers are 4.08, 3.96, and 3.91 Å, respectively. The decreasing tendency of
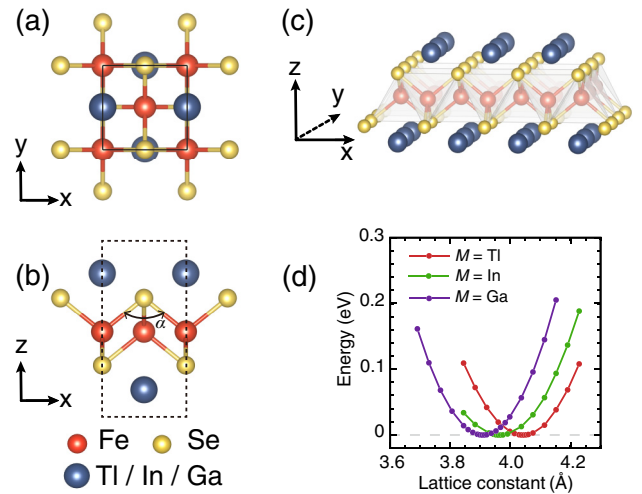

FIG. 1. (a), (b), and (c) Top, side, and oblique views, respectively, of the MFeSe (M = Tl, In, Ga) monolayers. Black lines in (a) indicate the boundaries of the unit cell. (d) Total energies as a function of the lattice constant for the three monolayers, in which the minimum total energy at the equilibrium lattice constant for each monolayer is set as energy zero.

the lattice constants for the three monolayers can be ascribed to the decrease of the atomic radius from Tl to Ga atoms. As listed in Table I, the nearest Fe-Fe distances and Fe-Se bond lengths for the three monolayers also have a decreasing tendency (Table I). The obtained cohesive energies for the TlFeSe, InFeSe, and GaFeSe monolayers are 2.89, 2.92, and 2.97 eV/atom (Table I). The positive and relatively large values of the cohesive energies of all the MFeSe indicate the very strong bonding between the atoms. Phonon spectra are calculated to check the dynamical stability of the monolayers, while MD simulations are performed to describe the thermal stability. As illustrated in Figs. 2(a)–2(c), no negative frequency is found in the whole BZ for all three monolayers built, manifesting the dynamical stability of the materials. The results of the MD simulations [Figs. 2(d)–2(f)] show that all the structures remain intact at 300 K after 10 ps. Thus, the three MFeSe (M = Tl, In, Ga) monolayers are all well stable at room temperature. Although the studied MFeSe (M = Tl, In, Ga) monolayers have not been synthesized in experiments yet, they might be fabricated with currently prosperous growth techniques in the future, such as chemical vapor transport technology [49,50] or intercalating M metal atoms into the layered FeSe film [19–22] and then exfoliating the film into

TABLE I. Calculated optimized lattice constants (a), nearest Fe-Fe distances ($d_{\text{Fe-Fe}}$), Fe-Se bond lengths ($d_{\text{Fe-Se}}$), vertical distances between the two M atomic planes (h), Fe-Se-Fe angles [α; see Fig. 1(b)], cohesive energies (E_c) for the MFeSe (M = Tl, In, Ga) monolayers.

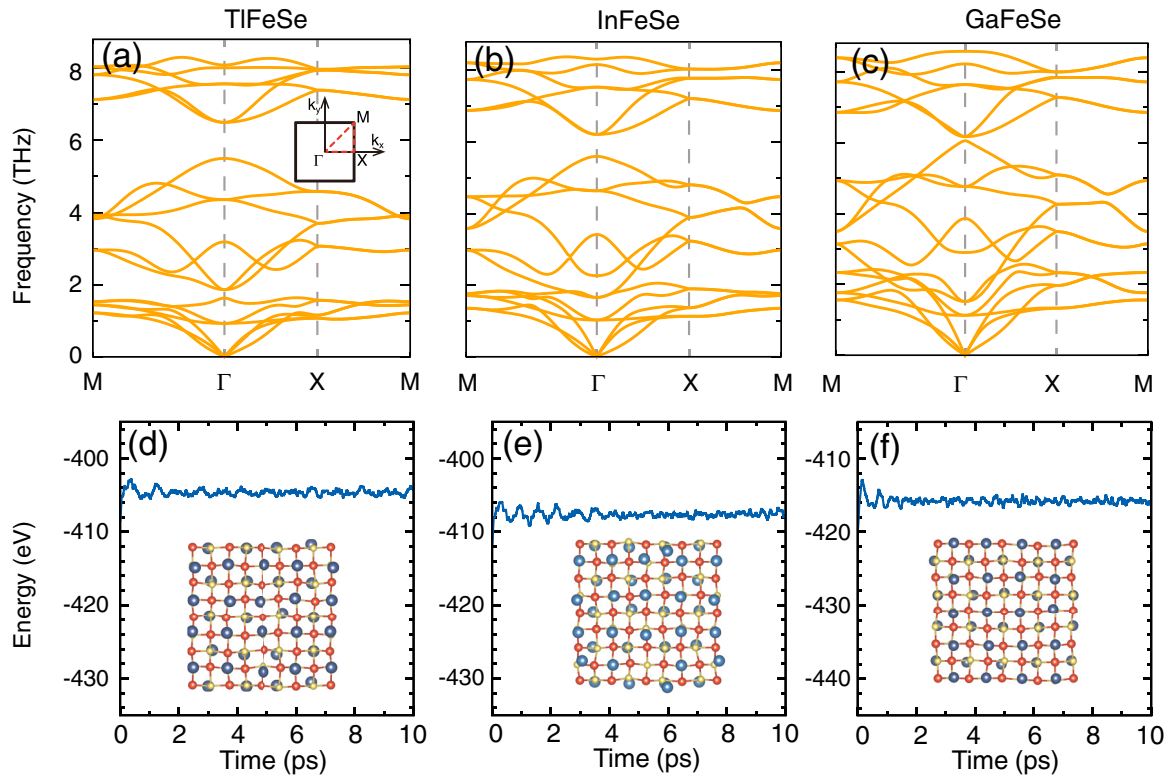|	a (Å)	$d_{\text{Fe-Fe}}$ (Å)	$d_{\text{Fe-Se}}$ (Å)	h (Å)	α (°)	E_c (eV/atom)
TlFeSe	4.08	2.88	3.19	5.77	106.4	2.89
InFeSe	3.96	2.80	3.10	5.84	102.6	2.92
GaFeSe	3.91	2.76	2.94	5.28	100.5	2.97

FIG. 2. (a)–(c) Phonon spectra of the TlFeSe, InFeSe, and GaFeSe monolayers, respectively. In (a), the first BZ is shown. (d)–(f) Energy evolution curves for the TlFeSe, InFeSe, and GaFeSe monolayers, respectively. In (d)–(f), the insets display snapshots of the final frames for the corresponding monolayers.

monolayers etc. The high quality of the synthesized materials is required for observing the phenomena obtained in this work.

We now explore the magnetic ground states for the MFeSe (M = Tl, In, Ga) monolayers. The total energies for the three monolayers with FM and five typical antiferromagnetic (AFM1-AFM5) configurations are calculated. The different magnetic configurations considered are illustrated in Fig. S1 in the Supplemental Material [51]. As listed in Table S1 in the Supplemental Material [51], for all three monolayers, the total energies for the FM configurations are lower than those of the AFM configurations by at least 2.0 eV per supercell. Thus, all three monolayers have FM ground states. Since magnetism generally originates from transition-metal elements frequently with partially filled d shell, the d-orbital projected band structures of the TlFeSe monolayer are shown as an example in Figs. 3(a) and 3(b) to discuss the magnetism. Obviously, the bands around the E_F are dominated by spin-down Fe d orbitals. The two linear spin-down bands cross at the E_F, resulting in the formation of a WHSM in the monolayer without the consideration of SOC.

The partial densities of states (DOSs) for the TlFeSe monolayer are displayed in Fig. S2 in the Supplemental Material [51]. The complete overlap of the DOSs of Fe d_{xz} and d_{yz} orbitals can be ascribed to the D_{4h} point group possessed in the monolayer. The DOSs of Se (Tl) p_x and p_y have the same behaviors. As shown in Fig. S2 in the Supplemental Material [51], both Tl $6p$ orbital and Fe $4s$ orbital donate one electron to Se $4p$, giving rise to Se $4p$ orbitals almost fully filled (Fig. S2(b) in the Supplemental Material [51]). And, the

FM magnetism in TlFeSe primarily comes from Fe $3d$ orbitals because the Fe spin-up $3d$ orbitals are almost fully filled, while its spin-down $3d$ orbitals are only partially occupied (Fig. S2(a) in the Supplemental Material [51]), leading to a net magnetic moment acquired in the monolayer. The role of the Tl atom in the monolayer is to primarily supply one electron to the Se atom, similar to the metal atoms, such as Li, K, Tl, intercalated into the layered FeSe materials [23–25,52]. After giving one electron to the Se atom, the Fe atom becomes an Fe^+ ion with a valence configuration of $3d^7 4s^0$, confirmed by the Bader charge calculations [53]. Note that one of the $4s$ electrons of Fe^+ transfers to Fe $3d$ can be attributed to the orbital hybridization, observed in other 2D material systems [54,55]. The occupation of the seven Fe $3d$ electrons on the orbitals is illustrated in Fig. 3(c). The d-orbital splitting order in Fig. 3(c) can be comprehended based on the crystal-field effect in square planar complexes whose energy order is $d_{x^2-y^2} > d_{xy} > d_{xz/yz} > d_{z^2}$. As the Se^{2-} ions in TlFeSe rise from the xy plane, they make the $d_{xz/yz}$ orbitals have a higher energy. After the exchange interaction is introduced, the spin-up and spin-down channels are split, leaving three $3d$ orbitals ($d_{x^2-y^2}$, $d_{xz/yz}$) half filled [Fig. 3(c)] and yielding a net magnetic moment of 3 μ_B per Fe atom.

According to Mermin-Wagner theorem [56], a long-range magnetic order is generally forbidden in isotropic one-dimensional or 2D systems at nonzero temperatures. Hence, magnetic anisotropy is crucial for a 2D material keeping in a long-range FM ground state. The total energies of MFeSe (M = Tl, In, Ga) with the magnetization direction along
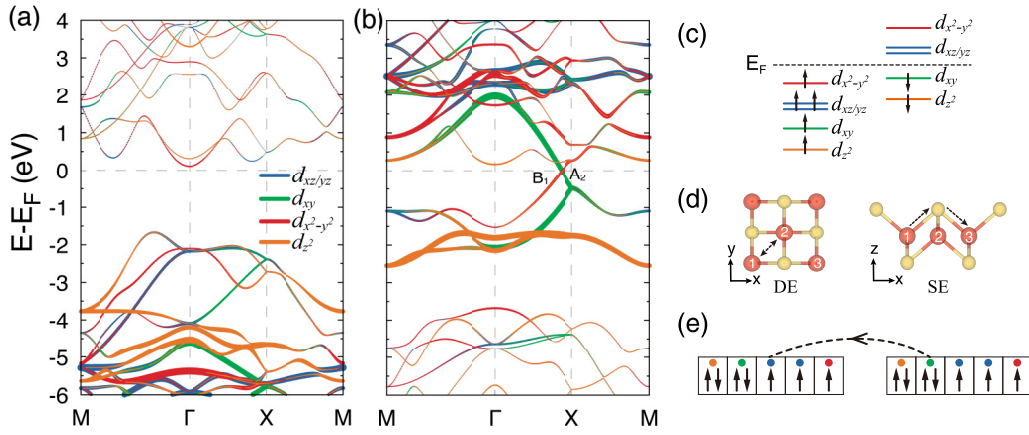
FIG. 3. (a), (b) d-orbital resolved band structures in spin-up and spin-down channels of the TlFeSe monolayer, respectively. The SOC is not considered. (c) Schematic diagram of the d-orbital distribution of Fe atoms at Γ point in the TlFeSe monolayer. (d) Schematic diagrams for the DE and SE coupling between the nearest-neighbor Fe1-Fe2 and the next-nearest-neighbor Fe1-Fe3 atoms, respectively. (e) Schematic diagram of the FM DE coupling between two nearest-neighbor Fe atoms in which the d orbitals are nearly fully filled.

[001], [100], and [110] are calculated and listed in Table II, where the lowest total energy of each monolayer is set as zero. Obviously, the total energy of the TlFeSe (and also GaFeSe) monolayer with the magnetization direction lying along the [100] direction (namely the x axis) is the lowest, compared to those of the material with the other two magnetization directions. Thus, the easy axis of magnetization for TlFeSe and GaFeSe is parallel to the xy plane. Differently, the easy axis of the InFeSe monolayer prefers the z axis. For TlFeSe, the total energies as a function of the angle (θ) between the magnetization direction within the xz plane and the x axis is plotted in Fig. 4(a), which can be described by the following equation [57]:

$$E(\theta) = E_e + K_1 \sin^2\theta + K_2 \sin^4\theta. \quad (1)$$

In Eq. (1), E_e is the total energy of the monolayer with the magnetization direction along the easy axis, set as zero. And, K_1 and K_2 are quadratic and quartic constants, respectively. For TlFeSe, K_1 and K_2 are 4.82 and 4.24 meV, respectively. As shown in Fig. 4(a) (and also Table II), very evident magnetic anisotropy with a magnetic anisotropy energy (MAE) of 9.05 meV is obtained for the TlFeSe monolayer. The calculated MAEs for InFeSe and GaFeSe are 0.23 and 0.59 meV, respectively (see Table II). The largest MAE achieved in TlFeSe can be ascribed to the largest SOC interaction in TlFeSe, containing the heavy Tl atoms. The obvious magnetic

anisotropy in the monolayers is beneficial to stabilize the FM ground states against the thermal fluctuation.

To evaluate the T_c of the three monolayers studied, a Heisenberg model is built. The Hamiltonian is written as

$$H_0 = -J_1 \sum_{\langle i,j \rangle} \mathbf{S}_i \cdot \mathbf{S}_j - J_2 \sum_{\langle\langle i,j \rangle\rangle} \mathbf{S}_i \cdot \mathbf{S}_j - D \sum_i \left| S_i^e \right|^2, \quad (2)$$

where $\mathbf{S}_i$ is the spin vector at the site i, S_i^e is the spin component along the easy axis, and D is the uniaxial anisotropy energy. Both the first and second terms can be regarded as isotropic exchange interactions. In Eq. (2), J_1 and J_2 express the parameters of the exchange interactions between the nearest-neighbor (NN) and the next-nearest-neighbor (NNN) Fe atoms, respectively. They are determined by comparing the total energies of the materials with the FM, AFM1, and AFM5 magnetic structures, in which the local magnetic moments of the Fe atoms are close to each other for each monolayer. The J_1, J_2, and D values can be calculated with following equations:

$$E_{FM} = E_0 - (16J_1 + 16J_2)|\mathbf{S}|^2, \quad (3)$$

$$E_{AFM1} = E_0 + 8J_2|\mathbf{S}|^2, \quad (4)$$

$$E_{AFM5} = E_0 + (16J_1 - 16J_2)|\mathbf{S}|^2, \quad (5)$$

$$D = [E_{max}(\text{axis}) - E_{easy}(\text{axis})]/(2|\mathbf{S}|^2), \quad (6)$$

where E_0 is the ground-state energy independent of the spin configuration, $\mathbf{S}$ is considered as a unit vector for convenience, and D denotes the MAE per Fe ion. The calculated results of J_1, J_2, and D are listed in Table II. Clearly, J_1 is significantly larger than J_2, both of which are positive, giving rise to FM ground states for all the MFeSe (M = Tl, In, Ga) monolayers. The temperature-dependent magnetization and specific heat for the MFeSe monolayers are shown in Figs. 4(b) and S3 in the Supplemental Material [51]. Phase transitions occur at the peaks of the specific-heat curves, indicating the T_c of 980, 1090, and 1280 K for the TlFeSe, InFeSe, and GaFeSe monolayers, respectively. To confirm the T_c values, another set of T_c is obtained from the configurations of FM, AFM4, and AFM5, with the values of 1070 K for TlFeSe, 1250 K for InFeSe, and

TABLE II. For MFeSe (M = Tl, In, Ga), the relative total energies (meV per unit cell) in different magnetization directions, magnetic coupling parameters of J_1 and J_2 (meV), anisotropic parameter D (meV per Fe atom), critical temperature T_c (K) obtained from the Heisenberg model, and electronic states obtained.

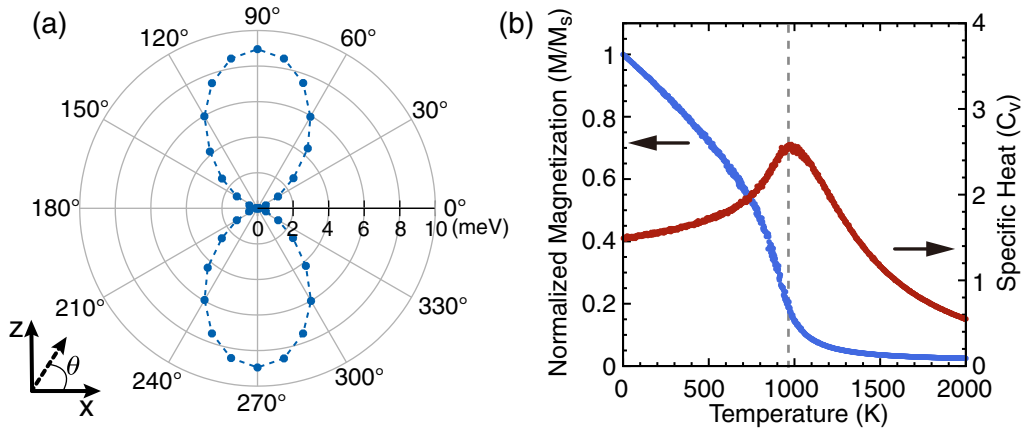| System	E_{001}	E_{100}	E_{110}	J_1	J_2	D	T_c	State
TlFeSe	9.05	0.00	0.04	95.75	21.29	4.53	980	WHSM
InFeSe	0.00	0.23	0.24	113.70	18.72	0.12	1090	QAH
GaFeSe	0.59	0.00	0.03	123.16	28.49	0.30	1280	WHSM

FIG. 4. (a) Total energies per unit cell of the TlFeSe monolayer as a function of the angle (θ). (b) Normalized average magnetic moment (blue curve) and specific heat (red curve) vs temperature for the TlFeSe monolayer.

1460 K for GaFeSe. The T_c values of both sets are close to each other, revealing the reliability of the T_c values obtained. Therefore, the predicted T_c values for the three monolayers are significantly higher than the room temperature and also than that of the 2D star magnetic material of the CrI$_3$ monolayer (45 K [58] or 95 K [59]).

The very high T_c values for the three monolayers are associated with the special geometric structure of the parent FeSe monolayer, supporting strong FM direct exchange (DE) and superexchange (SE) interactions in the MFeSe (M = Tl, In, Ga) monolayer materials [Fig. 3(d)]. In Figs. 1(a)–1(c), the NN Fe-Fe distances for the three monolayers are all very short, less than 3 Å (Table I), which favor a large overlapping of the d orbitals between the NN Fe atoms. In general, the NN [Fe1-Fe2 in Fig. 3(d)] DE interactions tend to be FM if the d orbitals are nearly fully filled [57] because the electrons are allowed to hop between the occupied and empty orbitals with the same spin component. This mechanism is illustrated in Fig. 3(e). Meanwhile, according to the Goodenough-Kanamori-Anderson (GKA) SE rule [60–62], the SE interactions between the NNN Fe atoms via the Se 4p orbitals, namely Fe1-Se-Fe3 in Fig. 3(d), are also FM. As listed in Table I, the bond angles (α) of Fe1-Se-Fe3 in MFeSe (M = Tl, In, Ga) are 106.4°, 102.6°, and 100.5°, respectively, close to the 90°. Both the DE and SE with FM interactions lead to the MFeSe (M = Tl, In, Ga) monolayers possessing very high T_c values. In many 2D FM materials, such as the CrI$_3$ [59] or XBr$_3$ (X = Cu, Ag, Au) [63] monolayers, the FM interactions of the SE coupling are partly canceled by the AFM interactions of the DE coupling, resulting in relatively low T_c values.

B. Weyl half semimetals and effective $k \cdot p$ model

We now investigate the electronic band structures of the MFeSe (M = Tl, In, Ga) monolayers. Figure 5 shows the calculated band structures of the three monolayers without and with the consideration of SOC. In the upper panel (without SOC), linear crosses formed by two spin-down bands are observed at the E_F for all three monolayers, which connect the conduction and valence bands. Thus, half metals [64], with 100% spin polarization, are acquired for all three monolayers

in the absence of SOC. Similar to the spin-down bands of the TlFeSe monolayer [Fig. 3(b)], the crosses of the InFeSe and GaFeSe monolayers are also primarily contributed by Fe spin-down d_{xy} and $d_{x^2-y^2}$ orbitals. After the SOC is turned on, the linear crosses at the E_F remain for the TlFeSe and GaFeSe monolayers [Figs. 5(d) and 5(f)] while the InFeSe monolayer [Fig. 5(e)] becomes a semiconductor with a band gap of 403 meV, due to the different easy-axis directions in these materials. Hence, 2D semimetals formed by completely spin-down bands are achieved for the TlFeSe and GaFeSe monolayers. Since the accidental band degeneracy of the crossing points is twofold, this type of semimetal is a Weyl semimetal. Due to the 100% spin polarization of the linear crosses at the E_F, the TlFeSe and GaFeSe monolayers can be called WHSMs [11–13], in analogy to the concept of half metals [64]. As illustrated in Figs. 5(d) and 5(f), both the WHSMs of TlFeSe and GaFeSe have large Fermi velocities. For example, the calculated Fermi velocity of the TlFeSe monolayer is 4.24×10^5 ms^{-1}, comparable to that of graphene ($\sim 1.0 \times 10^6$ ms^{-1}) [1,65]. These fully spin-polarized Weyl semimetals with very large Fermi velocities may be employed as FM electrode materials or FM materials to fabricate high-performance spin field-effect transistors [64] or magnetic tunnel junctions (MTJs) with 100% tunneling magnetoresistance [49] in spintronics.

The appearance of the Weyl points in TlFeSe and GaFeSe can be analyzed based on the symmetries possessed in the materials. The mechanism of the crossing points for the three monolayers in the absence of the SOC is first investigated. As shown in Figs. 5(a)–5(c), the crossing points are located in the Γ-X path at the E_F. Since all the monolayers have inversion symmetry P and rotational symmetry C_4, totally four Weyl points for each monolayer material can be found in the first BZ, along the -X-Γ-X and -Y-Γ-Y paths. As mentioned above, the Fe d_{xy} and $d_{x^2-y^2}$ orbitals in the spin-down channel constitute the crossing point. In the absence of the SOC, the spin and orbital degrees of freedom are decoupled, making spin a good quantum number in its own subspace. As such, the Γ-X path has the little group C_{2v} whose symmetry operators are E, $\tilde{C}_{2x} = \{C_{2x} \mid \frac{1}{2}, 0, 0\}$, $\tilde{M}_z = \{M_z \mid \frac{1}{2}, \frac{1}{2}, 0\}$, and $\tilde{M}_y = \{M_y \mid 0, \frac{1}{2}, 0\}$. The Hamiltonian ($H$) in an effective $k \cdot p$
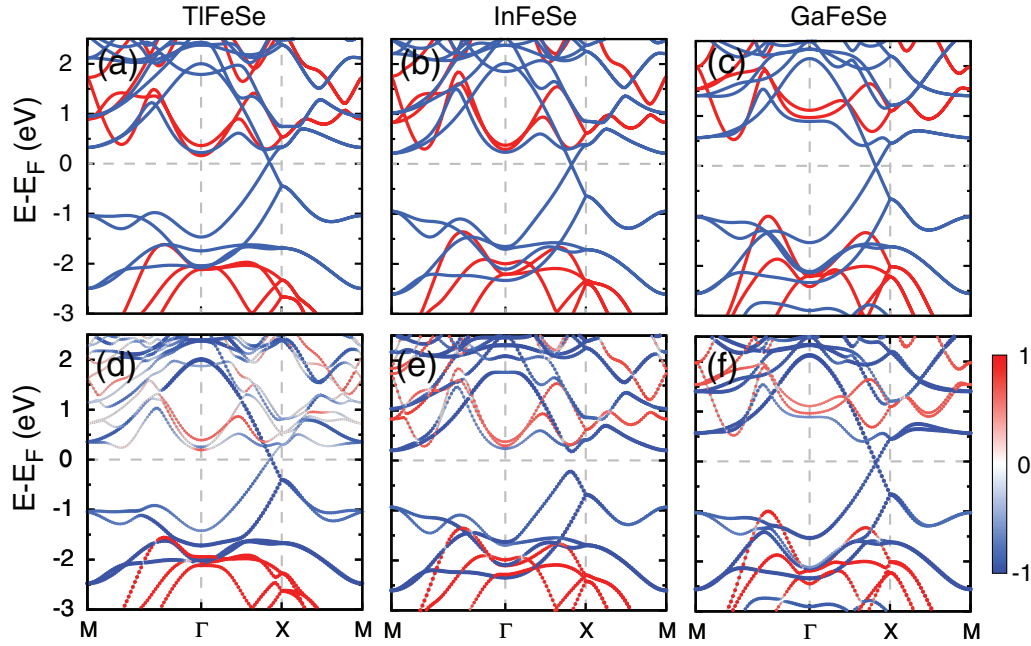
FIG. 5. (a)–(c) Band structures of the TlFeSe, InFeSe, and GaFeSe monolayers without SOC, respectively. The red and blue colors indicate the spin-up and spin-down bands, respectively. (d)–(f) Spin-resolved band structures of the TlFeSe, InFeSe, and GaFeSe monolayers in the presence of SOC, with the easy magnetization directions of the x, z, and x axes, respectively.

model can be constrained by

$$C_{2x}H(k_x, k_y)C_{2x}^{-1} = H(k_x, -k_y), \qquad (7)$$

$$M_zH(k_x, k_y)M_z^{-1} = H(k_x, k_y), \qquad (8)$$

$$M_yH(k_x, k_y)M_y^{-1} = H(k_x, -k_y). \qquad (9)$$

The H can, thus, be written as

$$H = A(k)\sigma_x + B(k)\sigma_y + C(k)\sigma_z + D(k)\sigma_0, \qquad (10)$$

where $A(k) = A_1k_y + A_2k_xk_y$, $B(k) = B_1k_y + B_2k_xk_y$, $C(k) = C_0 + C_1k_x + C_2k_x^2 + C_3k_y^2$, $D(k)=D_0 + D_1k_x+D_2k_x^2+D_3k_y^2$, $\sigma_x - \sigma_z$ are the Pauli matrixes, and σ_0 is the unit matrix. Note that Eq. (8) does not have constraints on the H and the $\tilde{C}_{2x}$ and $\tilde{M}_y$ symmetries have the same constraints on the H. By considering the first-order term and the condition of $D(k) = 0$, the degenerate point appears in $(-C_0/C_1, 0)$ along the Γ-X path ($k_y = 0$), rationalizing well the linear cross appearing in the Γ-X path for each monolayer material. Simultaneously, we also find that the two bands forming the crossing point belong to irreducible representations of B_1 and A_2, respectively [Fig. 3(b)], indicating from another perspective that the linear crosses in the MFeSe monolayers are protected by the symmetries the lattices possess.

After the SOC interaction is turned on, the existence of the crossing point depends on the magnetization directions. When the magnetization direction is along the x direction, the $\tilde{M}_y$ symmetry is broken but the $\tilde{C}_{2x}$ symmetry remains. Therefore, the $\tilde{C}_{2x}$ symmetry keeps the existence of the crossing points at the E_F as in TlFeSe [Fig. 5(d)] and GaFeSe [Fig. 5(f)], whose easy axes are both along the x direction. Thus, the crossing points at the E_F in TlFeSe and GaFeSe are robust against the SOC interaction. The Berry phase along a circular path around the crossing point in TlFeSe (and also GaFeSe) is calculated. Analogous to the Weyl points in the three-dimensional case

[66,67], a value of π is obtained, indicating the Weyl point holding a nonzero topological charge. For the InFeSe monolayer with an out-of-plane magnetization [Fig. 5(e)], both the $\tilde{C}_{2x}$ and $\tilde{M}_y$ symmetries in the system are broken. Hence, the Weyl point disappears. The InFeSe monolayer instead becomes a QAH state with a band gap (403 meV) opened around the E_F.

To identify the QAH phase predicted in InFeSe, the Chern number is calculated with following equation:

$$C = \frac{1}{2\pi} \int_{BZ} d^2k\Omega(k), \qquad (11)$$

where Ω is the Berry curvature in the reciprocal space. The distribution of the Berry curvatures in the k_x-k_y plane for the InFeSe monolayer is displayed in Fig. 6(a). Each of the four opening band gaps gives a topological charge of 0.5, resulting in a Chern number of 2 for InFeSe. The edge states (zigzag edge) of a semi-infinite InFeSe monolayer are calculated and shown in Fig. 6(b). Two chiral gapless edge states connect the valence and conduction bands, consistent with the results of $C = 2$. The analysis of the spin components demonstrates that the edge states are 100% spin polarized, giving a half-metallic behavior of the chiral edge states. Thus, spintronic devices such as MTJs [64] and spin filters [64] with very low dissipation may be made from the InFeSe monolayer. Additionally, the two chiral edge channels will transport the carriers in opposite directions if the magnetization direction in the material is reversed, which could be detected in experimental measurements.

In Figs. 5(a)–5(c), the bands in the X-M path all are twofold degenerate, where the SOC is not considered. The behavior can be rationalized well by the symmetry analysis. As mentioned above, the $P4/nmm$ space group owned in the MFeSe structure contains a screw-axis operation of
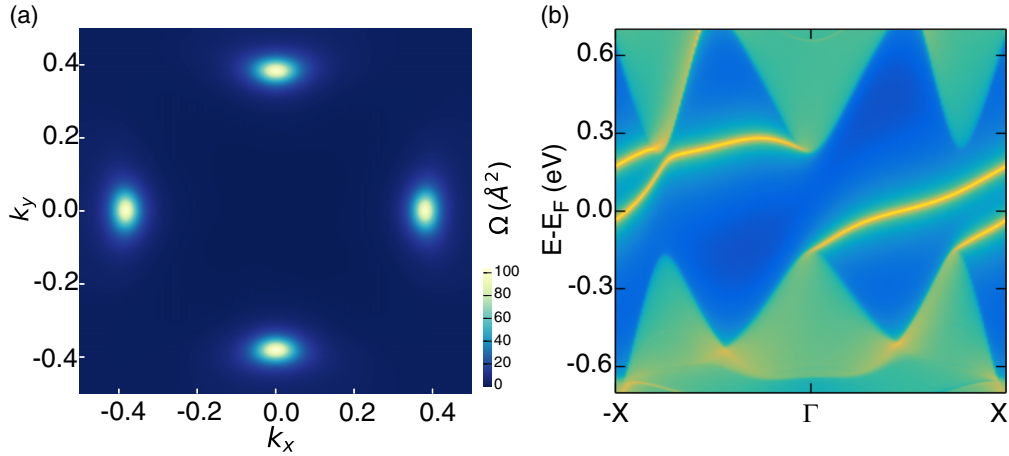
FIG. 6. (a) Distribution of the Berry curvatures in the k_x-k_y plane for the InFeSe monolayer. (b) Edge states of a semi-infinite InFeSe monolayer cut along the [100] direction.

$\tilde{C}_{2x} = \{C_{2x} \mid \frac{1}{2}, 0, 0\}$, with $\tilde{C}_{2x}^2 = e^{-ik_x}$. When $k_x = \pi$, we have $(TC_{2x})^2 = -1$. Therefore, all the bands along the X-M path ($k_x = \pi$) are Kramers-like degenerate [Figs. 5(a)–5(c)]. In the presence of the SOC, the time-reversal symmetry obeys $T^2 = -1$. When the magnetization direction is along the z axis [Fig. 5(e)], the system contains the twofold screw rotation combining with the time-reversal symmetry $T\tilde{C}_{2x}$. In this case, $\tilde{C}_{2x}^2 = -e^{-ik_x}$. Along the X-M path, we still have $(T\tilde{C}_{2x})^2 = -1$. Therefore, the double degeneracy of the bands in the X-M path in InFeSe with SOC [Fig. 5(e)] is protected by the $T\tilde{C}_{2x}$ combined symmetry. However, if the magnetization direction lies along the x axis, the $T\tilde{C}_{2x}$ symmetry is broken. And, the doubly degenerate bands split along the X-M path, as displayed in Figs. 5(d) and 5(f). At the X point of Figs. 5(d) and 5(f), the bands still maintain double degeneracy protected by a combined symmetry $T\tilde{M}_z$. As the $(T\tilde{M}_z)^2 = e^{-i(k_x+k_y)}$, we can obtain $(T\tilde{M}_z)^2 = -1$ with $(k_x, k_y) = (\pi, 0)$, which also leads to a Kramers-like double degeneracy at the X point.

C. Phase transitions between WHSMs and QAH states

Since magnetization directions of materials can be tuned by applying an external magnetic field [68,69], phase transitions between WHSMs and QAH states are expected in MFeSe (M = Tl, In, Ga) under magnetic fields. The band structures of the TlFeSe monolayer with the magnetization direction tuned from the x axis ($\theta = 0°$) to the z axis ($\theta = 90°$) are given in Figs. 7(a) and 7(b). The marked different irreducible representations of LD_3 and LD_4 in Fig. 7(a) confirm the double degeneracy of the crossing point in TlFeSe with the magnetization direction of $\theta = 0°$. However, when the magnetization direction is changed to the z axis, the Weyl point disappears and a band gap of 270 meV is opened [Fig. 7(b)], similar to the case of InFeSe [Fig. 5(e)]. The calculated Berry curvatures (Fig. S4(a) in the Supplemental Material [51]), Chern number ($C = 2$), and the edge states (Fig. S4(b) in the Supplemental Material [51]) prove that the TlFeSe with $\theta = 90°$ is a QAH insulator.

The calculated band gaps and Chern numbers vary continuously with the angle θ for the TlFeSe, InFeSe, and GaFeSe monolayers are illustrated in Figs. 7(c) and 7(d). For TlFeSe and GaFeSe, when $\theta = 0°$ and $180°$, WHSMs are achieved. Otherwise, QAH insulators with $C = 2$ are obtained due to the breakdown of the $T\tilde{C}_{2x}$ combined symmetry. The TlFeSe and GaFeSe monolayers with $\theta = 90°$ both have the maximum band gaps of 270 and 324 meV, respectively. The phase transition for InFeSe is somewhat different, from which we find that the Chern number of InFeSe changes from 2 to -2 when $\theta > 180°$ [Fig. 7(d)]. The critical state of a WHSM is acquired when $\theta = 180°$ for InFeSe. Thus, by rotating the magnetization direction, the materials can transform from a Weyl semimetal to a QAH insulator (TlFeSe and GaFeSe) or oppositely (InFeSe). The phase transition is associated with the combined symmetry of $T\tilde{C}_{2x}$ owned or not in the materials.

As indicated in Figs. 7(c) and 7(d), the band gap of the QAH state in TlFeSe with $\theta = 90°$ is the smallest (270 meV), compared to those in InFeSe (403 meV) and GaFeSe (324 meV). The trend is counterintuitive since the band gap of TlFeSe is expected to be the largest due to the heavy Tl element having a strong SOC effect. The reason can be understood from the spin-resolved band structures of the three monolayers with the magnetization directions all along the z axis (Fig. S5 in the Supplemental Material [51]). From GaFeSe to InFeSe, the unoccupied spin-up d_{z^2} orbitals (marked by an arrow in Figs. S5(b) and S5(c) in the Supplemental Material [51]) move down in energy. It becomes the bottom of the conduction bands in the case of TlFeSe (Fig. S5(a) in the Supplemental Material [51]), causing the decrease of the band gap in TlFeSe. If this band inversion is not considered, the band gap of TlFeSe ($\sim$430 meV), marked by two dashed lines in Fig. S5(a) in the Supplemental Material [51], is the largest among the three monolayers.

IV. CONCLUSIONS

A family of 2D high-temperature ferromagnetic monolayers of MFeSe (M = Tl, In, Ga) has been proposed. The structural stability, magnetic, and topologically electronic properties of these three materials are studied based on
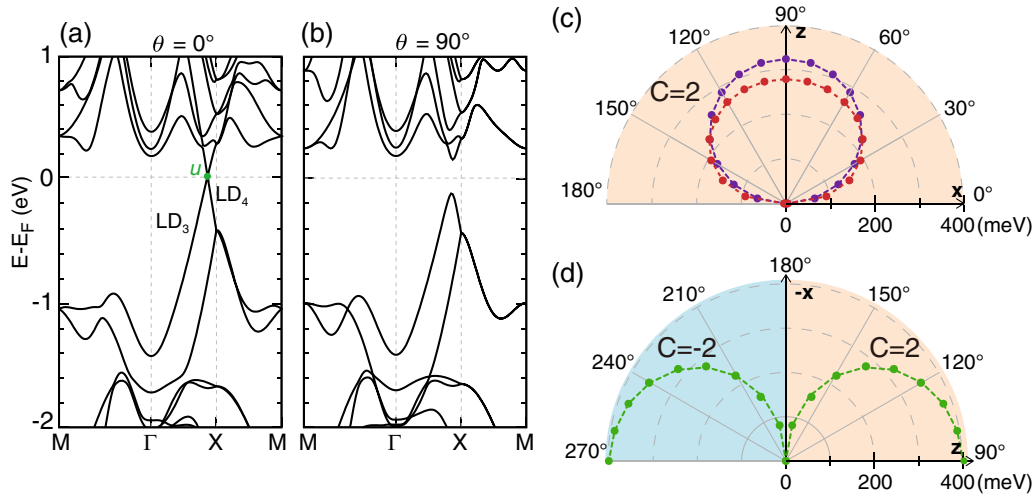
FIG. 7. (a) Band structure of the TlFeSe monolayer with the magnetization along the x axis ($\theta = 0°$). The irreducible representations of the two bands crossing the E_F are displayed. The crossing point u is indicated by a green dot. (b) Same as (a) except for $\theta = 90°$. The SOC is included in (a) and (b). (c) Band gaps of the TlFeSe (red dots) and GaFeSe (violet dots) monolayers with the magnetization direction varying from $\theta = 0°$ (easy axis) to $\theta = 180°$ in the xz plane. (d) Band gaps of the InFeSe monolayer with the magnetization direction varying from $\theta = 90°$ (easy axis) to $\theta = 270°$ in the xz planes. The light-brown and blue areas indicate the monolayers with Chern numbers of 2 and -2, respectively.

density-functional theory, $\boldsymbol{k} \cdot \boldsymbol{p}$ model, and symmetry analysis. We find that the TlFeSe and GaFeSe monolayers are stable candidates for 2D Weyl half semimetals and the InFeSe monolayer is an intrinsic QAH insulator with the band gap of 403 meV. The achieved T_c values for the monolayers are very high, up to 1280 K (for GaFeSe), rationalized by strong FM interactions through not only the NN Fe-Fe direct exchange coupling but also the NNN Fe-Fe superexchange coupling mediated by Se atoms. The Fermi velocity of the TlFeSe monolayer is up to 4.24×10^5 ms^{-1} which is useful for designing high-speed spintronic devices. By tuning the magnetization direction, the screw-axis symmetry can be broken in the monolayers, resulting in QAH states with various band gaps and a Chern number of 2 or -2. Our findings expand the iron-chalcogenide-based materials into topological materials and provide a promising platform for spintronics, topological superconductivity, and quantum computing.

[1] A. H. Castro Neto, F. Guinea, N. M. R. Peres, K. S. Novoselov, and A. K. Geim, Rev. Mod. Phys. **81**, 109 (2009).

[2] Q. H. Wang, K. Kalantar-Zadeh, A. Kis, J. N. Coleman, and M. S. Strano, Nat. Nanotechnol. **7**, 699 (2012).

[3] X. Lin, W. Yang, K. L. Wang, and W. Zhao, Nat. Electron. **2**, 274 (2019).

[4] E. C. Ahn, npj 2D Mater. Appl. **4**, 17 (2020).

[5] Y. Liu, C. Zeng, J. Zhong, J. Ding, Z. M. Wang, and Z. Liu, Nanomicro Lett. **12**, 93 (2020).

[6] G. Hu and B. Xiang, Nanoscale Res. Lett. **15**, 226 (2020).

[7] A. A. Burkov and L. Balents, Phys. Rev. Lett. **107**, 127205 (2011).

[8] C.-K. Chiu, J. C. Y. Teo, A. P. Schnyder, and S. Ryu, Rev. Mod. Phys. **88**, 035005 (2016).

[9] X. Dai, Nat. Phys. **12**, 727 (2016).

[10] N. P. Armitage, E. J. Mele, and A. Vishwanath, Rev. Mod. Phys. **90**, 015001 (2018).

[11] J.-Y. You, C. Chen, Z. Zhang, X.-L. Sheng, S. A. Yang, and G. Su, Phys. Rev. B **100**, 064408 (2019).

[12] G.-G. Li, R.-R. Xie, L.-J. Ding, W.-X. Ji, S.-S. Li, C.-W. Zhang, P. Li, and P.-J. Wang, Phys. Chem. Chem. Phys. **23**, 12068 (2021).

[13] L. Jin, L. Wang, X. Zhang, Y. Liu, X. Dai, H. Gao, and G. Liu, Nanoscale **13**, 5901 (2021).

[14] H. Huan, Y. Xue, B. Zhao, G. Gao, H. Bao, and Z. Yang, Phys. Rev. B **104**, 165427 (2021).

[15] X. Zhou, R.-W. Zhang, Z. Zhang, W. Feng, Y. Mokrousov, and Y. Yao, npj Comput. Mater. **7**, 160 (2021).

[16] J.-Y. You, Z. Zhang, B. Gu, and G. Su, Phys. Rev. Appl. **12**, 024063 (2019).

[17] T. Jia, W. Meng, H. Zhang, C. Liu, X. Dai, X. Zhang, and G. Liu, Front. Chem. **8**, 722 (2020).

[18] C.-L. Song, Y.-L. Wang, Y.-P. Jiang, Z. Li, L. Wang, K. He, X. Chen, X.-C. Ma, and Q.-K. Xue, Phys. Rev. B **84**, 020503(R) (2011).

[19] M.-H. Fang, H.-D. Wang, C.-H. Dong, Z.-J. Li, C.-M. Feng, J. Chen, and H. Q. Yuan, Europhys. Lett. **94**, 27009 (2011).

[20] T. P. Ying, X. L. Chen, G. Wang, S. F. Jin, T. T. Zhou, X. F. Lai, H. Zhang, and W. Y. Wang, Sci. Rep. **2**, 426 (2012).

[21] T. Hatakeda, T. Noji, T. Kawamata, M. Kato, and Y. Koike, J. Phys. Soc. Jpn. **82**, 123705 (2013).

[22] M. Burrard-Lucas, D. G. Free, S. J. Sedlmaier, J. D. Wright, S. J. Cassidy, Y. Hara, A. J. Corkett, T. Lancaster, P. J. Baker, S. J. Blundell, and S. J. Clarke, Nat. Mater. **12**, 15 (2013).

[23] S. He, J. He, W. Zhang, L. Zhao, D. Liu, X. Liu, D. Mou, Y.-B. Ou, Q.-Y. Wang, Z. Li, L. Wang, Y. Peng, Y. Liu, C. Chen, L. Yu, G. Liu, X. Dong, J. Zhang, C. Chen, Z. Xu, X. Chen, X. Ma, Q. Xue, and X. J. Zhou, Nat. Mater. **12**, 605 (2013).

[24] S. Tan, Y. Zhang, M. Xia, Z. Ye, F. Chen, X. Xie, R. Peng, D. Xu, Q. Fan, H. Xu, J. Jiang, T. Zhang, X. Lai, T. Xiang, J. Hu, B. Xie, and D. Feng, Nat. Mater. **12**, 634 (2013).

[25] J.-F. Ge, Z.-L. Liu, C. Liu, C.-L. Gao, D. Qian, Q.-K. Xue, Y. Liu, and J.-F. Jia, Nat. Mater. **14**, 285 (2015).

[26] K. He, Y. Wang, and Q.-K. Xue, Annu. Rev. Condens. Matter Phys. **9**, 329 (2018).

[27] Y. Ren, Z. Qiao, and Q. Niu, Rep. Prog. Phys. **79**, 066501 (2016).

[28] M. König, S. Wiedmann, C. Brüne, A. Roth, H. Buhmann, L. W. Molenkamp, X.-L. Qi, and S.-C. Zhang, Science **318**, 766 (2007).

[29] C. L. Kane and E. J. Mele, Phys. Rev. Lett. **95**, 226801 (2005).

[30] P. Chen, W. W. Pai, Y. H. Chan, W. L. Sun, C. Z. Xu, D. S. Lin, M. Y. Chou, A. V. Fedorov, and T. C. Chiang, Nat. Commun. **9**, 2003 (2018).

[31] Q.-Y. Wang, Z. Li, W.-H. Zhang, Z.-C. Zhang, J.-S. Zhang, W. Li, H. Ding, Y.-B. Ou, P. Deng, K. Chang, J. Wen, C.-L. Song, K. He, J.-F. Jia, S.-H. Ji, Y.-Y. Wang, L.-L. Wang, X. Chen, X.-C. Ma, and Q.-K. Xue, Chin. Phys. Lett. **29**, 037402 (2012).

[32] D. Liu, W. Zhang, D. Mou, J. He, Y.-B. Ou, Q.-Y. Wang, Z. Li, L. Wang, L. Zhao, S. He, Y. Peng, X. Liu, C. Chen, L. Yu, G. Liu, X. Dong, J. Zhang, C. Chen, Z. Xu, J. Hu, X. Chen, X. Ma, Q. Xue, and X. J. Zhou, Nat. Commun. **3**, 931 (2012).

[33] X. Liu, L. Zhao, S. He, J. He, D. Liu, D. Mou, B. Shen, Y. Hu, J. Huang, and X. J. Zhou, J. Phys.: Condens. Matter **27**, 183201 (2015).

[34] G. Kresse and J. Furthmüller, Phys. Rev. B **54**, 11169 (1996).

[35] G. Kresse and J. Furthmüller, Comput. Mater. Sci. **6**, 15 (1996).

[36] G. Kresse and D. Joubert, Phys. Rev. B **59**, 1758 (1999).

[37] A. V. Krukau, O. A. Vydrov, A. F. Izmaylov, and G. E. Scuseria, J. Chem. Phys. **125**, 224106 (2006).

[38] H. Weng, C. Fang, Z. Fang, B. A. Bernevig, and X. Dai, Phys. Rev. X **5**, 011029 (2015).

[39] S.-Y. Xu, I. Belopolski, N. Alidoust, M. Neupane, G. Bian, C. Zhang, R. Sankar, G. Chang, Z. Yuan, C.-C. Lee, S.-M. Huang, H. Zheng, J. Ma, D. S. Sanchez, B. Wang, A. Bansil, F. Chou, P. P. Shibayev, H. Lin, S. Jia, and M. Z. Hasan, Science **349**, 613 (2015).

[40] A. Jesche, N. Caroca-Canales, H. Rosner, H. Borrmann, A. Ormeci, D. Kasinathan, H. H. Klauss, H. Luetkens, R. Khasanov, A. Amato, A. Hoser, K. Kaneko, C. Krellner, and C. Geibel, Phys. Rev. B **78**, 180504(R) (2008).

[41] K. Liu, B.-J. Zhang, and Z.-Y. Lu, Phys. Rev. B **91**, 045107 (2015).

[42] H. J. Monkhorst and J. D. Pack, Phys. Rev. B **13**, 5188 (1976).

[43] A. Togo and I. Tanaka, Scr. Mater. **108**, 1 (2015).

[44] G. Pizzi, V. Vitale, R. Arita, S. Blugel, F. Freimuth, G. Geranton, M. Gibertini, D. Gresch, C. Johnson, T. Koretsune, J. Ibanez-Azpiroz, H. Lee, J. M. Lihm, D. Marchand, A. Marrazzo, Y. Mokrousov, J. I. Mustafa, Y. Nohara, Y. Nomura, L. Paulatto, S. Ponce, T. Ponweiser, J. F. Qiao, F. Thole, S. S. Tsirkin, M. Wierzbowska, N. Marzari, D. Vanderbilt, I. Souza, A. A. Mostofi, and J. R. Yates, J. Phys.: Condens. Matter **32**, 165902 (2020).

[45] Q. Wu, S. Zhang, H.-F. Song, M. Troyer, and A. A. Soluyanov, Comput. Phys. Commun. **224**, 405 (2018).

[46] R. F. L. Evans, W. J. Fan, P. Chureemart, T. A. Ostler, M. O. A. Ellis, and R. W. Chantrell, J. Phys.: Condens. Matter **26**, 103202 (2014).

[47] H. K. Vivanco and E. E. Rodriguez, J. Solid State Chem. **242**, 3 (2016).

[48] I. A. Nekrasov, N. S. Pavlov, M. V. Sadovskii, and A. A. Slobodchikov, Low Temp. Phys. **42**, 891 (2016).

[49] Y. Jin, M. Yan, Y. Dedkov, and E. Voloshina, J. Mater. Chem. C **10**, 3812 (2022).

[50] T. Zhang, Y. Wang, H. Li, F. Zhong, J. Shi, M. Wu, Z. Sun, W. Shen, B. Wei, W. Hu, X. Liu, L. Huang, C. Hu, Z. Wang, C. Jiang, S. Yang, Q.-m. Zhang, and Z. Qu, ACS Nano **13**, 11353 (2019).

[51] See Supplemental Material at http://link.aps.org/supplemental/10.1103/PhysRevB.106.125404 for the different magnetic structures and the corresponding total energies, projected DOSs for TlFeSe, normalized average magnetic moments and specific heats for InFeSe and GaFeSe, Berry curvatures and edge states for TlFeSe with $\theta = 90°$, and spin-resolved band structures for the MFeSe (M = {Tl}, In, Ga) monolayers with $\theta = 90°$.

[52] Y. Li, J. Li, Y. Li, M. Ye, F. Zheng, Z. Zhang, J. Fu, W. Duan, and Y. Xu, Phys. Rev. Lett. **125**, 086401 (2020).

[53] M. Yu and D. R. Trinkle, J. Chem. Phys. **134**, 064111 (2011).

[54] C. Cao, M. Wu, J. Jiang, and H.-P. Cheng, Phys. Rev. B **81**, 205424 (2010).

[55] T. O. Wehling, A. I. Lichtenstein, and M. I. Katsnelson, Phys. Rev. B **84**, 235110 (2011).

[56] N. D. Mermin and H. Wagner, Phys. Rev. Lett. **17**, 1133 (1966).

[57] J. M. D. Coey, *Magnetism and Magnetic Materials* (Cambridge University Press, Cambridge, 2010).

[58] B. Huang, G. Clark, E. Navarro-Moratalla, D. R. Klein, R. Cheng, K. L. Seyler, D. Zhong, E. Schmidgall, M. A. McGuire, D. H. Cobden, W. Yao, D. Xiao, P. Jarillo-Herrero, and X. Xu, Nature (London) **546**, 270 (2017).

[59] W.-B. Zhang, Q. Qu, P. Zhu, and C.-H. Lam, J. Mater. Chem. C **3**, 12457 (2015).

[60] J. B. Goodenough, Phys. Rev. **100**, 564 (1955).

[61] P. W. Anderson, Phys. Rev. **115**, 2 (1959).

[62] J. Kanamori, J. Appl. Phys. **31**, S14 (1960).

[63] X. Liu, J. Zhang, Y. Wang, H. Bao, Y. Qi, and Z. Yang, J. Mater. Chem. C **10**, 6497 (2022).

[64] I. Žutić, J. Fabian, and S. Das Sarma, Rev. Mod. Phys. **76**, 323 (2004).

[65] D. C. Elias, R. V. Gorbachev, A. S. Mayorov, S. V. Morozov, A. A. Zhukov, P. Blake, L. A. Ponomarenko, I. V. Grigorieva, K. S. Novoselov, F. Guinea, and A. K. Geim, Nat. Phys. **7**, 701 (2011).

[66] N. Nagaosa, T. Morimoto, and Y. Tokura, Nat. Rev. Mater. **5**, 621 (2020).

[67] S. Bravo, M. Pacheco, V. Nuñez, J. D. Correa, and L. Chico, Nanoscale **13**, 6117 (2021).

[68] S. Nie, Y. Sun, F. B. Prinz, Z. Wang, H. Weng, Z. Fang, and X. Dai, Phys. Rev. Lett. **124**, 076403 (2020).

[69] M. Wu, 2D Mater. **4**, 021014 (2017).